ACS Photonics

Article

Cite This: ACS Photonics 2018, 5, 5010−5016

pubs.acs.org/journal/apchd5

Monolithic On-chip Magneto-optical Isolator with 3 dB Insertion Loss and 40 dB Isolation Ratio

Qingyang Du,[†,⊥] Chuangtang Wang,[‡,⊥] Yifei Zhang,[†] Yan Zhang,[†,‡] Takian Fakhrul,[†] Wei Zhang,[§] Claudia Gonçalves,[∥] Cesar Blanco,[∥] Kathleen Richardson,[∥] Longjiang Deng,[‡] Caroline A. Ross,[†] Lei Bi,[*,‡] and Juejun Hu[*,†]

[†]Department of Materials Science and Engineering, Massachusetts Institute of Technology, Cambridge, Massachusetts 02139, United States

[‡]State Key Laboratory of Electronic Thin Films and Integrated Devices, University of Electronic Science and Technology of China, Chengdu 610054, China

[§]Key Laboratory of Photoelectric Detection Materials and Devices of Zhejiang Province, Ningbo University, Ningbo 315211, China

[∥]The College of Optics & Photonics, University of Central Florida, Orlando, Florida 32816, United States

Supporting Information

ABSTRACT: On-chip optical isolators constitute an essential building block for photonic integrated circuits (PICs). Here, we experimentally demonstrated a magneto-optical isolator monolithically integrated on silicon featuring 3 dB insertion loss and 40 dB isolation ratio, both of which represent significant improvements over state-of-the-art. The isolator is also fully passive and operates under a simple unidirectional magnetization scheme. Such superior performance is enabled through a three-way combination of a strip-loaded waveguide design, a compositionally optimized chalcogenide glass as the light guiding medium, and low-loss taper structures created via gray -scale lithographic processing. The device represents an important step toward a practical solution for on-chip isolation in PICs.

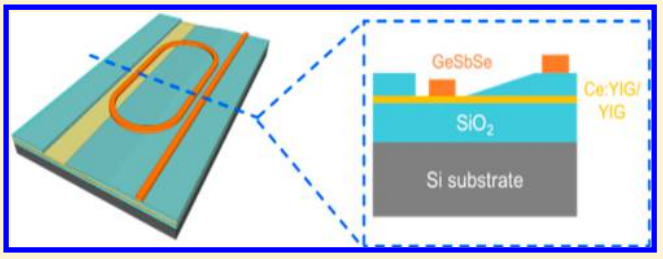

KEYWORDS: *Isolators, magneto-optical materials, integrated optics devices, resonators, chalcogenide glass, grayscale-lithography*

An isolator is a nonreciprocal device that permits optical transmission in only one direction through breaking the time-reversal symmetry of light propagation.[1] Such nonreciprocal optical transmission can be achieved leveraging a variety of mechanisms including magneto-optical effects,[2−24] optical nonlinearity,[25−29] dynamic modulation,[30−33] and optomechanical interactions.[34] Among these approaches, magneto-optical isolation benefits from its fully passive operation, simple device architectures, and large dynamic range, and therefore, it has been the incumbent solution adopted in current bulk optical systems.

In planar photonic integrated circuits (PICs), an optical isolator also represents an essential building block as it suppresses detrimental feedback between different components due to unwanted reflections and stabilizes the operation of PICs. Implementing magneto-optical isolation on-chip, nevertheless, has been a challenging task. Magneto-optical garnets used in bulk isolator devices, exemplified by bismuth or cerium substituted yttrium iron garnet (Bi:YIG, $Bi_xY_{3-x}Fe_5O_{12}$; Ce:YIG, $Ce_xY_{3-x}Fe_5O_{12}$), suffer from large lattice and coefficient of thermal expansion (CTE) mismatches with common semiconductor substrates. As a result, integration of these materials on semiconductors relies on either hybrid bonding of garnet crystals[12−19] or direct deposition of polycrystalline films.[6−11] Compared to hybrid bonding, the monolithic approach offers a significantly simplified processing route. However, monolithic isolator devices based on deposited garnet materials so far only exhibit suboptimal performances in terms of isolation ratio (IR, the ratio between forward and backward transmittances, Figure 1a) and insertion loss (IL, optical loss of forward propagating light through the isolator device, Figure 1a), the two most important metrics for optical isolators. The largest IR to date in monolithic isolators, 19.5 dB, was attained in a nonreciprocal resonator near 1550 nm wavelength, which is unfortunately accompanied by an excessive IL of 18.8 dB.[6] A recently demonstrated quasi-phase-matched Faraday rotator achieves a reduced IL of 4.6 dB albeit with a lower IR of 11 dB.[11] These figures are far inferior compared to their free-space bulk counterparts, which claim ILs below 0.5 dB and IRs of around 40 dB at the telecommunication band.[35] It is therefore imperative to create new device solutions to narrow the performance gap if monolithic isolators are to secure a place in next-generation PICs.

Received: September 6, 2018
Published: November 21, 2018

DOI: 10.1021/acsphotonics.8b01257
ACS Photonics 2018, 5, 5010−5016

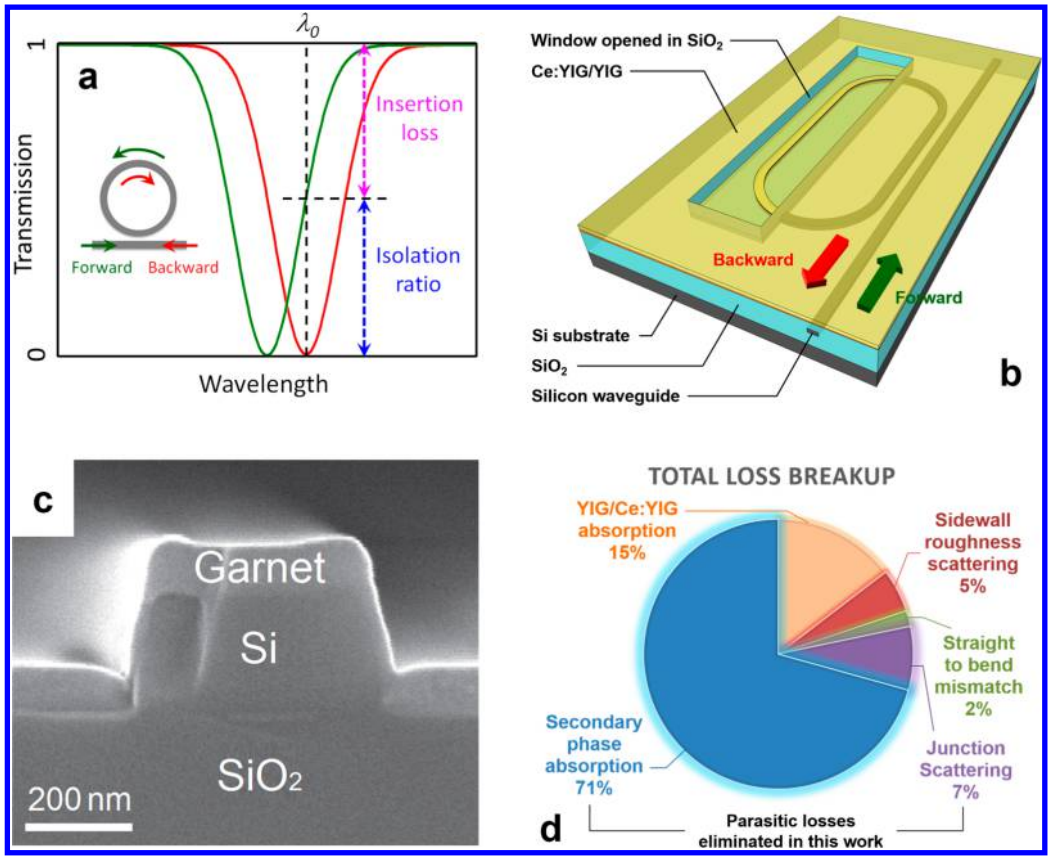

Figure 1. (a) Schematic transmission spectra of a resonator isolator; (b) resonator isolator structure demonstrated in ref 6; (c) cross-sectional SEM image of a SOI waveguide covered with deposited magneto-optical oxides (ref 6); (d) breakup of loss contributions in the isolator device in ref 6.

It is worth pointing out that the quality of deposited polycrystalline garnet films is not the main performance-limiting factor in these early prototypes. For instance, Faraday rotation (FR) up to 2650 deg/cm (measured at saturation magnetization) has been obtained in deposited ferrimagnetic Ce:YIG films,[36] approaching values measured in single-crystalline films of similar compositions.[37,38] Admittedly, optical loss of the deposited Ce:YIG films (40 dB/cm at 1550 nm[39]) is still considerably higher than that of their single-crystalline counterpart (<10 dB/cm[37]). The material figure-of-merit (material FOM, defined as the ratio between FR and material loss) reaches 66 deg/dB even with such relatively high material losses, which predicts an IL down to 0.8 dB for a Faraday rotator if parasitic losses (other than material attenuation) are absent; far superior compared to the experimentally obtained performance. Understanding the nonidealities that account for such subpar device characteristics is thus critical to further improving on-chip isolator performances.

In this Article, we report the experimental demonstration of a monolithic on-chip isolator exhibiting an IL as low as 3.0 dB and an IR exceeding 40 dB, both of which represent major improvements over state-of-the-art. Such unprecedented performance builds on our understanding of the optical loss mechanisms in prior isolator devices and implementation of corresponding loss mitigation strategies, which we present in the next section. A novel isolator architecture based on strip-loaded waveguide structures with adiabatic vertical tapers was applied to eliminate the parasitic losses. Design, fabrication, and characterization of the device are elaborated in the succeeding sections.

Optical Loss Mechanism Analysis. Figure 1b schematically illustrates the layout of a resonator-based magneto-optical isolator. When a magnetic field is applied, degeneracy between the clockwise and counterclockwise propagating modes of the resonator is lifted due to nonreciprocal phase shift (NRPS) in the magneto-optically active waveguide, leading to asymmetric transmission in the bus waveguide for forward and backward propagating light. The sign of NRPS depends on the direction of magnetization with respect to the light propagation direction. Therefore, unidirectional magnetization of an *entire* closed-loop resonator leads to vanishing resonance splitting since NRPS on opposite sides of the resonator has different signs and cancels out. This issue can be resolved either by applying a radial magnetic field to each resonator, or keeping only *part* of the resonator magneto-optically active. Radial magnetization demands a needle-shaped magnet[17] or an electromagnetic microcoil[18] to be placed in close proximity to each and every resonator, considerably increasing device complexity.

The approach of maintaining magneto-optical activity in only part of the resonator was previously implemented by opening a window in the resonator top cladding prior to garnet film deposition such that the magneto-optical film only contacts the waveguide core in the window region. Figure 1c shows a cross-sectional scanning electron microscopy (SEM) image of a silicon-on-insulator (SOI) waveguide covered with deposited garnet films fabricated using the approach.[6] In this prototypical device, the deposited film consists of a bottom unsubstituted yttrium iron garnet (YIG) buffer layer and a Ce:YIG layer on top, the latter of which is the main magneto-optically active medium. The unsubstituted YIG buffer layer,

DOI: 10.1021/acsphotonics.8b01257
ACS Photonics 2018, 5, 5010−5016

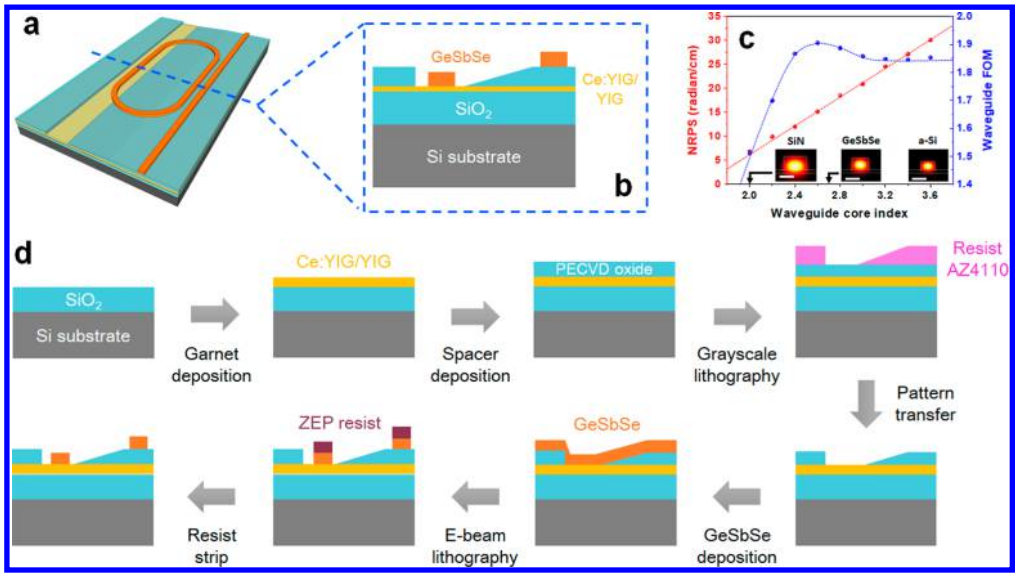

Figure 2. (a) Tilted-view and (b) cross-sectional schematic of the new isolator design; (c) nonreciprocal phase shift and waveguide figure of merit computed as functions of the strip-loaded waveguide core refractive index: the insets are modal profiles of strip-loaded waveguides when the core material is chosen as silicon nitride (n = 2.0), GeSbSe glass (n = 2.7), and amorphous silicon (n = 3.6), where the scale bars correspond to 500 nm; (d) fabrication process flow for the isolator device.

which readily crystallizes into the garnet phase and subsequently serves as a template promoting Ce:YIG crystallization, is essential to obtaining a high-quality Ce:YIG film. Our prior work has revealed that when thickness of the YIG buffer layer is reduced to below a certain threshold value, crystallization of the top Ce:YIG layer into the magneto-optically active garnet phase is hindered.[40]

The device configuration, however, incurs two undesired sources of parasitic loss. First of all, we found that it was more difficult to fully crystallize garnet films deposited on substrates with sidewall topography (e.g., waveguides) and observed greater formation of secondary phases such as iron oxide with unacceptably high optical absorption and decreased magneto-optical activity. This may be a consequence of the reduced total film thickness (and hence YIG buffer layer thickness) on the sidewalls compared to the film on top of the waveguide, as is evident from Figure 1c. This issue cannot be resolved by simply increasing the overall film thickness, as the stack thickness is bound by CTE mismatch to no more than a few hundred nanometers.[41] Furthermore, the windows opened in the waveguide cladding for garnet deposition introduce junctions with abrupt index changes, causing significant scattering losses.

Figure 1d illustrates the different loss contributions in the isolator device in ref 6. Details of the loss estimates are compiled in the Supporting Information. Clearly, parasitic absorption resulting from secondary phases and scattering loss at the junctions are the major contributors accounting for 80% of the total loss. In the next section, we focus on an isolator architecture designed to eliminate these parasitic losses.

Isolator Design and Fabrication. The new isolator design is depicted in Figure 2a (perspective view) and 2b (cross-section). The basic building block of the isolator is a nonreciprocal magneto-optical resonator comprising strip-loaded waveguides on a deposited Ce:YIG film. The film is deposited on a planar silica-on-silicon layer and is fully crystallized into the garnet phase (confirmed by X-ray diffraction and vibrating sample magnetometry measurements) with low optical loss. By sandwiching a vertically tapered oxide spacer layer between the strip-loaded waveguide core and the Ce:YIG film, only a fraction of the microring is in direct contact with the Ce:YIG layer and magneto-optically active. The oxide taper creates an adiabatic mode transformer, which minimizes scattering and Fresnel reflection losses between waveguide sections with and without the spacer layer. The design therefore eliminates the two dominant sources of parasitic optical losses, i.e., absorption from secondary phases and waveguide junction scattering, which underpins the superior isolation performance we experimentally obtained in the device.

The design also features an added benefit through enhancing nonreciprocity in the waveguide. The unsubstituted YIG seed layer exhibits Faraday rotation with a sign opposite to that of Ce:YIG,[36] which partially cancels out the waveguide NRPS. The deleterious effect is aggravated in the traditional waveguide structure as the YIG layer sits directly on top of the Si core, thereby having large spatial overlap with the evanescent field. In the strip-loaded waveguide configuration, the effect is alleviated since the Ce:YIG layer rather than the YIG layer is in direct contact with the waveguide core. Our numerical modeling suggests that the configuration contributes to a 26% enhancement in NRPS of the waveguide.

The isolator design is further optimized through judicious choice of the waveguide core material. Figure 2c plots the simulated NRPS and FOM of the strip-loaded waveguide on Ce:YIG as functions of the refractive index of the core material. Here, the waveguide FOM (a dimensionless quantity) is defined as

$$\mathrm{FOM_{WG}} = \frac{\Delta\beta}{\alpha} \tag{1}$$

where $\Delta\beta$ denotes the waveguide NRPS for the quasi-TM mode, i.e., the propagation constant difference of forward and backward propagating modes in the waveguide (in radian per cm), and α gives the waveguide propagation loss (in $\mathrm{cm^{-1}}$). The waveguide FOM scales with the material FOM defined in

DOI: 10.1021/acsphotonics.8b01257
ACS Photonics 2018, 5, 5010−5016

the previous section but additionally depends on the waveguide geometry, and ultimately dictates the performance of magneto-optical isolators.[8] In Figure 2c, the waveguide dimensions are optimized to achieve maximum waveguide FOM for each core material index value while ensuring single-mode operation. The corresponding waveguide design parameters are tabulated in the Supporting Information. The simulations show that, while NRPS monotonically rises with increasing refractive index of the core over the range of indices considered, modal confinement in the Ce:YIG layer and hence optical loss also grows as a result of the reduced core thickness and increasing field discontinuity at the boundaries. The trade-off therefore points to an optimal core index of 2.6 to reach the maximum waveguide FOM.

Based on this insight, we selected $Ge_{22}Sb_{18}Se_{60}$ (GeSbSe), a chalcogenide glass (ChG), as the waveguide core material. The glass has a refractive index of 2.7 near 1550 nm wavelength, close to the optimal value of 2.6. The chemical stability and optical transparency of GeSbSe glasses have also been experimentally established.[42,43] Moreover, we have already matured fabrication protocols for low-loss ChG photonic devices including on-chip resonators with quality factors (Q-factors) exceeding one million[44] and applied the technique to realize a wide array of functional photonic components and systems.[45−48] The low deposition and processing temperatures of ChG further mitigates the risk of film cracking or delamination due to thermal stress accumulation.[49] We note that the isolator architecture is, however, generic and can also make use of other low-loss deposited dielectric materials such as silicon nitride[50] and amorphous silicon[51] as the waveguide core. Additionally, the strip-loaded waveguide layout as well as the low-loss vertical taper structure are equally applicable to enhancing the performance of other isolator device platforms such as those based on Mach−Zehnder interferometers (MZIs). The process flow to fabricate the isolator structure is shown in Figure 2d.

Figure 3a shows a top-view optical microscope image of the fabricated resonator isolator, where the color fringes on the substrate manifest the gradual thickness variation of the oxide spacer layer. Figure 3b displays a cross-sectional SEM image of the ChG waveguide core sitting on the spacer layer in a region of device without the tapered spacer. The waveguide has nearly vertical sidewalls and a well-defined width of 650 nm, an optimized value following our numerical simulation results.

Isolator Characterization. Figure 4a illustrates a schematic diagram of the isolator characterization setup. The fabricated device was tested on a Newport Autoalign station where light was coupled in and out of the waveguides via end fire coupling through tapered fibers (Nanonics Imaging Ltd.) mounted on computerized motion stages. The device chip was covered with an index matching fluid (Cargille-Sacher Laboratories Inc.), which helps to minimize Fresnel reflection in fiber-to-chip coupling. An optical vector analyzer (OVA, Luna Innovations Inc.) with built-in external cavity tunable laser was used in conjunction with an erbium-doped fiber amplifier (Amonics Ltd.) as the interrogation light source. The waveguide output spectrum was also monitored by the OVA. During the test, a rare-earth permanent magnet was placed near one end of the device chip to impose a nearly unidirectional magnetic field of approximately 0.1 T on the devices, sufficient to saturate the magnetization of the ferrimagnetic Ce:YIG film. The isolation performance was validated by reversing the light propagation direction. The

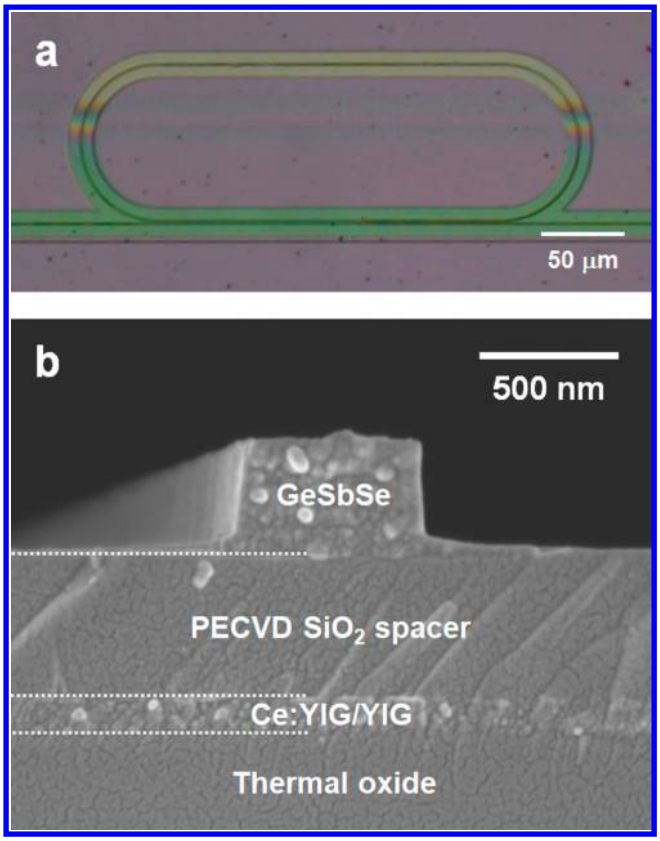

Figure 3. (a) Top-view optical micrograph of a fabricated resonator isolator; (b) cross-sectional SEM image of the strip-loaded waveguide showing the layer structures.

measurement was repeated five consecutive times and averaged to suppress unwanted resonant peak drift due to temperature fluctuations.

The bidirectional transmission spectra of quasi-TM mode in the isolator device are presented in Figure 4b. As shown in the figure, the device exhibits an IL as low as 3.0 dB and a high IR of 40 dB, both of which set the performance records for monolithic magneto-optical isolators. The spectra, averaged over five consecutive measurements, reveal a nonreciprocal resonant peak shift of (44 ± 4) pm, in agreement with our simulation results. The resonant peak positions at both forward and backward directions recorded during the five repeated measurements are plotted in Figure 4c. Wavelength dependence of the nonreciprocal resonance shift was characterized in the wavelengths range of 1540 to 1590 nm. The measurement results, plotted in Figure 4d alongside theoretical simulations, indicate a nearly wavelength-independent nonreciprocal resonance shift resulting from two opposing contributions: at longer wavelengths, the diminished FR of Ce:YIG[52] is balanced by a wavelength squared dependence of nonreciprocal resonance shift (refer to the Supporting Information for details of the simulations and further discussions).

Based on the isolator characterization outcome, we quantified the different factors contributing to the overall loss in the device. Total loss in the nonreciprocal resonator is computed from the measured loaded Q-factor and extinction ratio to be 17.5 dB/cm, representing over 70% reduction compared to our prior report.[6] Propagation loss of GeSbSe racetrack resonators without the underlying magneto-optical oxide layers but with an otherwise identical configuration was

DOI: 10.1021/acsphotonics.8b01257
ACS Photonics 2018, 5, 5010−5016

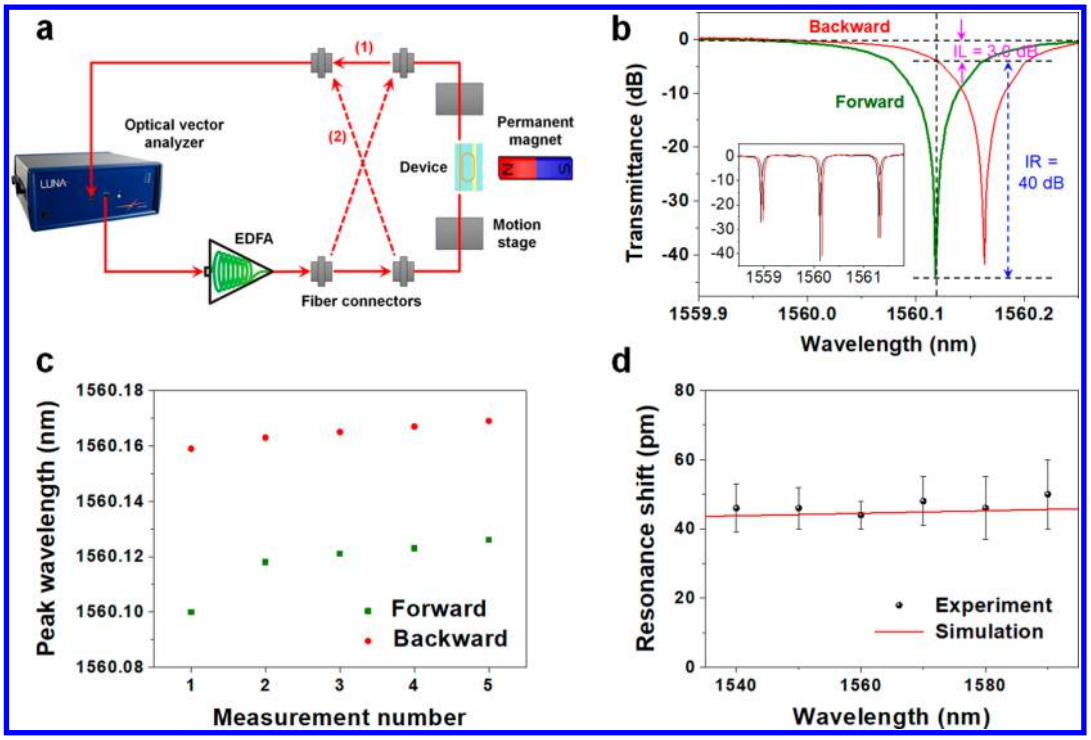

Figure 4. (a) Experimental setup for characterization of the isolator device: (1) and (2) indicate optical paths used to interrogate the device in forward and backward propagating directions, respectively; (b) transmission spectra of the isolator: inset shows the same spectra over several free spectral ranges of the resonator; (c) resonant peak wavelengths of the device repeatedly measured for five consecutive times; (d) spectral dispersion of the nonreciprocal resonant wavelength shift measured in the isolator.

experimentally assessed to be 3.8 dB/cm, among which 1.1 dB/cm is attributed to scattering losses at the four straight-to-bend junctions in the racetrack resonator according to our finite-difference time-domain (FDTD) simulations. Such scattering losses can be easily eliminated by replacing the circular segments in the racetrack with a curve that has a continuous curvature change along its length, such as Euler spiral or Bezier curve.[53,54] The remaining 2.7 dB/cm, presumably resulting from sidewall roughness scattering in the GeSbSe waveguide, is higher than the 0.5 dB/cm loss value we previously measured in ChG microring resonators,[44] indicating considerable room for further performance improvement. Loss caused by optical absorption in the magneto-optical oxide films is therefore 13.7 dB/cm, corresponding to 270 dB/cm absorption in the magneto-optical oxides. This figure is considerably higher than loss we previously measured in polycrystalline Ce:YIG films (40 dB/cm at 1550 nm[39]). We thus anticipate that the IL of monolithic on-chip isolators can be further minimized with optimized garnet deposition protocols to bring their performance to a level on par with or even superior to their bulk counterparts.

It worth pointing out that the narrow working bandwidth of the resonator-based isolator precludes their application with broadband tunable lasers. When used in conjunction with single-wavelength lasers (which represents most use cases in PICs), the device's isolation wavelength can be tuned to match the laser emitting wavelength by thermo-optic locking or photosensitive trimming, an added benefit of using ChGs as the waveguide material.[55] In addition, the strip-loaded magneto-optical waveguide design coupled with low-loss vertical tapers is equally applicable to reducing loss in broadband interferometer isolators, and therefore, our approach will likely have a broad impact on on-chip isolator integration.

CONCLUSION

In this article, we have significantly advanced the state-of-the-art in monolithic integrated optical isolators by demonstrating an on-chip isolator with a record low insertion loss of 3.0 dB and an isolation ratio of 40 dB. The exceptional isolation performance stems from a novel device architecture combining a strip-loaded waveguide configuration with an adiabatic vertical taper, which effectively eliminates parasitic optical losses due to secondary phase absorption and junction scattering while, at the same time, boosting waveguide nonreciprocity. The high-performance, all-passive on-chip isolator constitutes a critical step toward planar integration of optical isolation devices with large-scale photonic circuits.

METHODS

MO Material Deposition. Si wafers coated with 3 μm wet oxide (MTI Corp.) were used as the substrate. The wafers were first cleaned in a piranha bath to remove contaminants. A 50 nm unsubstituted YIG layer was then deposited onto the substrate using pulsed laser deposition (PLD) at a substrate temperature of 400 °C and an oxygen pressure of 5 mTorr. The as-deposited YIG film is amorphous, and the film was subsequently rapid thermal annealed at 850 °C for 2 min to form a polycrystalline seed layer. A 90 nm Ce:YIG film was deposited onto the seed layer at a substrate temperature of 750 °C and 10 mTorr O_2 pressure using PLD. Composition of the film was quantified using inductively coupled plasma mass spectrometry (ICP-MS) to be $Ce_1Y_2Fe_5O_{12}$. The Ce:YIG film formed at the temperature spontaneously crystallizes during growth facilitated by the unsubstituted YIG seed layer.

DOI: 10.1021/acsphotonics.8b01257
ACS Photonics 2018, 5, 5010−5016

Device Fabrication. A 500 nm silicon oxide spacer layer was deposited on top of Ce:YIG using plasma-enhanced chemical vapor deposition (PECVD) with a gas mixture of silane and N_2O at 500 mTorr pressure and a plasma power of 80 W. The oxide vertical taper structure was subsequently defined using grayscale lithography. The continuous-tone grayscale photomask was fabricated via electron beam writing in an off-the-shelf High Energy Beam Sensitive (HEBS) glass plate (Canyon Materials, Inc.). The writing dose was calibrated following standard calibration procedures detailed elsewhere.[56] During the grayscale lithography process, an AZ4110 photoresist (MicroChemicals GmbH) layer with 1 μm thickness was spin coated onto the substrate and baked at 100 °C for 1 min. The resist was exposed on a Karl Suss MA-4 mask aligner at a total dose of 100 mJ/cm^2 and then developed in AZ400K developer solution (with 1:3 dilution) for 30 s to produce the grayscale resist pattern. The pattern was subsequently transferred into the oxide layer via reactive ion etch (RIE) using a mixed etching gas of CF_4 and O_2 at 30 mTorr pressure and 200 W incident power to form the silicon dioxide vertical taper structure. The taper has a height of 500 nm and a width of 80 μm, corresponding to a taper angle of approximately 0.4°. The small taper angle ensures adiabatic mode transformation with negligible optical attenuation. A GeSbSe film of 360 nm thickness was thermally evaporated to function as the waveguide core layer. Patterning of the ChG waveguides followed previously established protocols that involve electron beam lithography and dry etching using a CHF_3 and CF_4 plasma[44] to complete the device fabrication.

■ ASSOCIATED CONTENT

Supporting Information

The Supporting Information is available free of charge on the ACS Publications website at DOI: 10.1021/acsphotonics.8b01257.

Detailed numerical analysis of isolator loss contributor, waveguide FR and FOM simulation, and wavelength dispersion of NRPS; comparison of this work to state-of-the-art PDF)

■ AUTHOR INFORMATION

Corresponding Authors

*E-mail: bilei@uestc.edu.cn.
*E-mail: hujuejun@mit.edu.

ORCID

Qingyang Du: 0000-0002-1424-356X
Caroline A. Ross: 0000-0003-2262-1249
Lei Bi: 0000-0002-2698-2829

Author Contributions

⊥These authors contributed equally to this work.

Funding

This work was partly supported by the National Science Foundation (NSF) under awards 1607865 and 1453218, and used shared experimental facilities of CMSE, an NSF MRSEC under award DMR1419807.

Notes

The authors declare no competing financial interest.

■ ACKNOWLEDGMENTS

The authors gratefully thank Lionel C. Kimerling and Anu Agarwal for providing access to device measurement facilities. The authors also acknowledge fabrication facility support by the MIT Microsystems Technology Laboratories.

■ REFERENCES

(1) Jalas, D.; Petrov, A.; Eich, M.; Freude, W.; Fan, S.; Yu, Z.; Baets, R.; Popović, M.; Melloni, A.; Joannopoulos, J. D. What is—and what is not—an optical isolator. *Nat. Photonics* **2013**, *7*, 579.

(2) Dötsch, H.; Bahlmann, N.; Zhuromskyy, O.; Hammer, M.; Wilkens, L.; Gerhardt, R.; Hertel, P.; Popkov, A. F. Applications of magneto-optical waveguides in integrated optics. *J. Opt. Soc. Am. B* **2005**, *22*, 240−253.

(3) Stadler, B. J.; Mizumoto, T. Integrated magneto-optical materials and isolators: a review. *IEEE Photonics J.* **2014**, *6*, 1−15.

(4) Bi, L.; Hu, J.; Jiang, P.; Kim, H. S.; Kim, D. H.; Onbasli, M. C.; Dionne, G. F.; Ross, C. A. Magneto-optical thin films for on-chip monolithic integration of non-reciprocal photonic devices. *Materials* **2013**, *6*, 5094−5117.

(5) Shoji, Y.; Mizumoto, T. Magneto-optical non-reciprocal devices in silicon photonics. *Sci. Technol. Adv. Mater.* **2014**, *15*, 014602.

(6) Bi, L.; Hu, J.; Jiang, P.; Kim, D. H.; Dionne, G. F.; Kimerling, L. C.; Ross, C. On-chip optical isolation in monolithically integrated non-reciprocal optical resonators. *Nat. Photonics* **2011**, *5*, 758.

(7) Bi, L.; Hu, J.; Kimerling, L.; Ross, C. In *Fabrication and characterization of $As_2S_3/Y_3Fe_5O_{12}$ and $Y_3Fe_5O_{12}$/SOI strip-loaded waveguides for integrated optical isolator applications*; Integrated Optics: Devices, Materials, and Technologies XIV; International Society for Optics and Photonics: 2010; p 760406.

(8) Sun, X. Y.; Du, Q.; Goto, T.; Onbasli, M. C.; Kim, D. H.; Aimon, N. M.; Hu, J.; Ross, C. A. Single-step deposition of cerium-substituted yttrium iron garnet for monolithic on-chip optical isolation. *ACS Photonics* **2015**, *2*, 856−863.

(9) Goto, T.; Onbasli, M. C.; Kim, D. H.; Singh, V.; Inoue, M.; Kimerling, L. C.; Ross, C. A nonreciprocal racetrack resonator based on vacuum-annealed magnetooptical cerium-substituted yttrium iron garnet. *Opt. Express* **2014**, *22*, 19047−19054.

(10) Hutchings, D. C.; Holmes, B. M.; Zhang, C.; Dulal, P.; Block, A. D.; Sung, S.-Y.; Seaton, N. C.; Stadler, B. J. Quasi-phase-matched faraday rotation in semiconductor waveguides with a magnetooptic cladding for monolithically integrated optical isolators. *IEEE Photonics J.* **2013**, *5*, 6602512−6602512.

(11) Zhang, C.; Dulal, P.; Stadler, B. J.; Hutchings, D. C. Monolithically-Integrated TE-mode 1D Silicon-on-Insulator Isolators using Seedlayer-Free Garnet. *Sci. Rep.* **2017**, *7*, 5820.

(12) Mizumoto, T.; Shoji, Y.; Takei, R. Direct wafer bonding and its application to waveguide optical isolators. *Materials* **2012**, *5*, 985−1004.

(13) Karki, D.; Stenger, V.; Pollick, A.; Levy, M. Thin-film magnetless Faraday rotators for compact heterogeneous integrated optical isolators. *J. Appl. Phys.* **2017**, *121*, 233101.

(14) Shoji, Y.; Mizumoto, T.; Yokoi, H.; Hsieh, I.-W.; Osgood, R. M., Jr Magneto-optical isolator with silicon waveguides fabricated by direct bonding. *Appl. Phys. Lett.* **2008**, *92*, 071117.

(15) Ghosh, S.; Keyvavinia, S.; Van Roy, W.; Mizumoto, T.; Roelkens, G.; Baets, R. Ce:YIG/Silicon-on-Insulator waveguide optical isolator realized by adhesive bonding. *Opt. Express* **2012**, *20*, 1839−1848.

(16) Ghosh, S.; Keyvaninia, S.; Shoji, Y.; Van Roy, W.; Mizumoto, T.; Roelkens, G.; Baets, R. G. Compact Mach−Zehnder interferometer Ce: YIG/SOI optical isolators. *IEEE Photonics Technol. Lett.* **2012**, *24*, 1653−1656.

(17) Tien, M.-C.; Mizumoto, T.; Pintus, P.; Kromer, H.; Bowers, J. E. Silicon ring isolators with bonded nonreciprocal magneto-optic garnets. *Opt. Express* **2011**, *19*, 11740−11745.

(18) Huang, D.; Pintus, P.; Zhang, C.; Morton, P.; Shoji, Y.; Mizumoto, T.; Bowers, J. E. Dynamically reconfigurable integrated optical circulators. *Optica* **2017**, *4*, 23−30.

(19) Huang, D.; Pintus, P.; Shoji, Y.; Morton, P.; Mizumoto, T.; Bowers, J. E. Integrated broadband Ce: YIG/Si Mach−Zehnder

DOI: 10.1021/acsphotonics.8b01257
ACS Photonics 2018, 5, 5010−5016

optical isolators with over 100 nm tuning range. *Opt. Lett.* **2017**, *42*, 4901−4904.
(20) Huang, D.; Pintus, P.; Zhang, C.; Shoji, Y.; Mizumoto, T.; Bowers, J. E. Electrically driven and thermally tunable integrated optical isolators for silicon photonics. *IEEE J. Sel. Top. Quantum Electron.* **2016**, *22*, 271−278.
(21) Ishida, E.; Miura, K.; Shoji, Y.; Yokoi, H.; Mizumoto, T.; Nishiyama, N.; Arai, S. Amorphous-Si waveguide on a garnet magneto-optical isolator with a TE mode nonreciprocal phase shift. *Opt. Express* **2017**, *25*, 452−462.
(22) Montoya, J.; Parameswaran, K.; Hensley, J.; Allen, M.; Ram, R. Surface plasmon isolator based on nonreciprocal coupling. *J. Appl. Phys.* **2009**, *106*, 023108.
(23) Shimizu, H.; Nakano, Y. Monolithic Integration of a Waveguide Optical Isolator With a Distributed Feedback Laser Diode in the 1.5-μm Wavelength Range. *IEEE Photonics Technol. Lett.* **2007**, *19*, 1973−1975.
(24) Levy, M.; Carroll, T. K.; El-Ganainy, R. Enhancing optical isolator performance in nonreciprocal waveguide arrays. *Opt. Lett.* **2015**, *40*, 111−114.
(25) Shi, Y.; Yu, Z.; Fan, S. Limitations of nonlinear optical isolators due to dynamic reciprocity. *Nat. Photonics* **2015**, *9*, 388−392.
(26) Fan, L.; Wang, J.; Varghese, L. T.; Shen, H.; Niu, B.; Xuan, Y.; Weiner, A. M.; Qi, M. An all-silicon passive optical diode. *Science* **2012**, *335*, 447−450.
(27) Chang, L.; Jiang, X.; Hua, S.; Yang, C.; Wen, J.; Jiang, L.; Li, G.; Wang, G.; Xiao, M. Parity−time symmetry and variable optical isolation in active−passive-coupled microresonators. *Nat. Photonics* **2014**, *8*, 524.
(28) Peng, B.; Özdemir, Ş. K.; Lei, F.; Monifi, F.; Gianfreda, M.; Long, G. L.; Fan, S.; Nori, F.; Bender, C. M.; Yang, L. Parity-time-symmetric whispering-gallery microcavities. *Nat. Phys.* **2014**, *10*, 394.
(29) Del Bino, L.; Silver, J. M.; Woodley, M. T.; Stebbings, S. L.; Zhao, X.; Del'Haye, P. Microresonator isolators and circulators based on the intrinsic nonreciprocity of the Kerr effect. *Optica* **2018**, *5*, 279−282.
(30) Yu, Z.; Fan, S. Complete optical isolation created by indirect interband photonic transitions. *Nat. Photonics* **2009**, *3*, 91.
(31) Lira, H.; Yu, Z.; Fan, S.; Lipson, M. Electrically driven nonreciprocity induced by interband photonic transition on a silicon chip. *Phys. Rev. Lett.* **2012**, *109*, 033901.
(32) Yang, Y.; Galland, C.; Liu, Y.; Tan, K.; Ding, R.; Li, Q.; Bergman, K.; Baehr-Jones, T.; Hochberg, M. Experimental demonstration of broadband Lorentz non-reciprocity in an integrable photonic architecture based on Mach-Zehnder modulators. *Opt. Express* **2014**, *22*, 17409−17422.
(33) Doerr, C.; Chen, L.; Vermeulen, D. Silicon photonics broadband modulation-based isolator. *Opt. Express* **2014**, *22*, 4493−4498.
(34) Manipatruni, S.; Robinson, J. T.; Lipson, M. Optical nonreciprocity in optomechanical structures. *Phys. Rev. Lett.* **2009**, *102*, 213903.
(35) IR Free-Space Isolators. https://www.thorlabs.com/newgrouppage9.cfm?objectgroup_id=4916 (accessed 04/25/2018).
(36) Onbasli, M. C.; Goto, T.; Sun, X.; Huynh, N.; Ross, C. Integration of bulk-quality thin film magneto-optical cerium-doped yttrium iron garnet on silicon nitride photonic substrates. *Opt. Express* **2014**, *22*, 25183−25192.
(37) Shintaku, T.; Tate, A.; Mino, S. Ce-substituted yttrium iron garnet films prepared on $Gd_3Sc_2Ga_3O_{12}$ garnet substrates by sputter epitaxy. *Appl. Phys. Lett.* **1997**, *71*, 1640−1642.
(38) Onbasli, M. C.; Beran, L.; Zahradník, M.; Kučera, M.; Antoš, R.; Mistrík, J.; Dionne, G. F.; Veis, M.; Ross, C. A. Optical and magneto-optical behavior of cerium yttrium iron garnet thin films at wavelengths of 200−1770 nm. *Sci. Rep.* **2016**, *6*, 23640.
(39) Bi, L.; Hu, J.; Dionne, G. F.; Kimerling, L.; Ross, C. In *Monolithic integration of chalcogenide glass/iron garnet waveguides and resonators for on-chip nonreciprocal photonic devices*; Integrated Optics: Devices, Materials, and Technologies XV; International Society for Optics and Photonics: 2011; p 794105.
(40) Goto, T.; Onbaşlı, M. C.; Ross, C. A. Magneto-optical properties of cerium substituted yttrium iron garnet films with reduced thermal budget for monolithic photonic integrated circuits. *Opt. Express* **2012**, *20*, 28507−28517.
(41) Sung, S.-Y.; Sharma, A.; Block, A.; Keuhn, K.; Stadler, B. J. H. Magneto-optical garnet waveguides on semiconductor platforms: Magnetics, mechanics, and photonics. *J. Appl. Phys.* **2011**, *109*, 07B738.
(42) Wei, W.-H.; Wang, R.-P.; Shen, X.; Fang, L.; Luther-Davies, B. Correlation between structural and physical properties in Ge−Sb−Se glasses. *J. Phys. Chem. C* **2013**, *117*, 16571−16576.
(43) Krogstad, M. R.; Ahn, S.; Park, W.; Gopinath, J. T. Nonlinear characterization of $Ge_{28}Sb_{12}Se_{60}$ bulk and waveguide devices. *Opt. Express* **2015**, *23*, 7870−7878.
(44) Du, Q.; Huang, Y.; Li, J.; Kita, D.; Michon, J.; Lin, H.; Li, L.; Novak, S.; Richardson, K.; Zhang, W. Low-loss photonic device in Ge−Sb−S chalcogenide glass. *Opt. Lett.* **2016**, *41*, 3090−3093.
(45) Du, Q.; Luo, Z.; Zhong, H.; Zhang, Y.; Huang, Y.; Du, T.; Zhang, W.; Gu, T.; Hu, J. Chip-scale broadband spectroscopic chemical sensing using an integrated supercontinuum source in a chalcogenide glass waveguide. *Photonics Res.* **2018**, *6*, 506−510.
(46) Li, L.; Lin, H.; Huang, Y.; Shiue, R.-J.; Yadav, A.; Li, J.; Michon, J.; Englund, D.; Richardson, K.; Gu, T. High-performance flexible waveguide-integrated photodetectors. *Optica* **2018**, *5*, 44−51.
(47) Lin, H.; Song, Y.; Huang, Y.; Kita, D.; Deckoff-Jones, S.; Wang, K.; Li, L.; Li, J.; Zheng, H.; Luo, Z. Chalcogenide glass-on-graphene photonics. *Nat. Photonics* **2017**, *11*, 798−805.
(48) Li, L.; Lin, H.; Qiao, S.; Zou, Y.; Danto, S.; Richardson, K.; Musgraves, J. D.; Lu, N.; Hu, J. Integrated flexible chalcogenide glass photonic devices. *Nat. Photonics* **2014**, *8*, 643−649.
(49) Hu, J.; Li, L.; Lin, H.; Zou, Y.; Du, Q.; Smith, C.; Novak, S.; Richardson, K.; Musgraves, J. D. Chalcogenide glass microphotonics: Stepping into the spotlight. *Am. Ceram. Soc. Bull.* **2015**, *94*, 24−29.
(50) Bauters, J. F.; Heck, M. J.; John, D.; Dai, D.; Tien, M.-C.; Barton, J. S.; Leinse, A.; Heideman, R. G.; Blumenthal, D. J.; Bowers, J. E. Ultra-low-loss high-aspect-ratio Si_3N_4 waveguides. *Opt. Express* **2011**, *19*, 3163−3174.
(51) Selvaraja, S. K.; Sleeckx, E.; Schaekers, M.; Bogaerts, W.; Van Thourhout, D.; Dumon, P.; Baets, R. Low-loss amorphous silicon-on-insulator technology for photonic integrated circuitry. *Opt. Commun.* **2009**, *282*, 1767−1770.
(52) Zhang, Y.; Wang, C.; Liang, X.; Peng, B.; Lu, H.; Zhou, P.; Zhang, L.; Xie, J.; Deng, L.; Zahradnik, M. Enhanced magneto-optical effect in $Y_{1.5}Ce_{1.5}Fe_5O_{12}$ thin films deposited on silicon by pulsed laser deposition. *J. Alloys Compd.* **2017**, *703*, 591−599.
(53) Cherchi, M.; Ylinen, S.; Harjanne, M.; Kapulainen, M.; Aalto, T. Dramatic size reduction of waveguide bends on a micron-scale silicon photonic platform. *Opt. Express* **2013**, *21*, 17814−17823.
(54) Li, L.; Lin, H.; Qiao, S.; Huang, Y.-Z.; Li, J.-Y.; Michon, J.; Gu, T.; Alosno-Ramos, C.; Vivien, L.; Yadav, A. Monolithically integrated stretchable photonics. *Light: Sci. Appl.* **2017**, *7*, 17138.
(55) Canciamilla, A.; Grillanda, S.; Morichetti, F.; Ferrari, C.; Hu, J.; Musgraves, J. D.; Richardson, K.; Agarwal, A.; Kimerling, L. C.; Melloni, A. Photo-induced trimming of coupled ring-resonator filters and delay lines in As_2S_3chalcogenide glass. *Opt. Lett.* **2011**, *36*, 4002.
(56) Dillon, T. E.; Sure, A.; Murakowski, J. A.; Prather, D. W. Continuous-tone grayscale mask fabrication using high-energy-beam-sensitive glass. *J. Micro/Nanolithogr., MEMS, MOEMS* **2004**, *3*, 550−555.

DOI: 10.1021/acsphotonics.8b01257
ACS Photonics 2018, 5, 5010−5016